

Carrier-induced transition from antiferromagnetic insulator to ferromagnetic metal in the layered phosphide EuZn_2P_2

Xiyu Chen,¹ Wuzhang Yang,^{2,3} Jia-Yi Lu,⁴ Zhiyu Zhou,¹ Zhi Ren,^{2,3} Guang-Han Cao,^{4,5} Shuai Dong,¹ and Zhi-Cheng Wang^{1,*}

¹Key Laboratory of Quantum Materials and Devices of Ministry of Education, School of Physics, Southeast University, Nanjing 211189, China

²School of Science, Westlake University, Hangzhou 310024, China

³Institute of Natural Sciences, Westlake Institute for Advanced Study, Hangzhou 310024, China

⁴School of Physics, Interdisciplinary Center for Quantum Information and State Key Laboratory of Silicon and Advanced Semiconductor Materials, Zhejiang University, Hangzhou 310058, China

⁵Collaborative Innovation Centre of Advanced Microstructures, Nanjing University, Nanjing 210093, China

(Dated: June 11, 2024)

EuZn_2P_2 was reported to be an insulating antiferromagnet with T_N of 23.5 K. In this study, single crystals of EuZn_2P_2 exhibiting metallic behavior and a ferromagnetic order of 72 K (T_C) are successfully synthesized via a salt flux method. The presence of hole carriers induced by the Eu vacancies in the lattice is found to be crucial for the drastic changes in magnetism and electrical transport. The carriers mediate the interlayer ferromagnetic interaction, and the coupling strength is directly related to T_C , as evidenced by the linear dependence of T_C and the fitted Curie-Weiss temperatures on the Eu-layer distances for ferromagnetic EuM_2X_2 ($M = \text{Zn}, \text{Cd}; X = \text{P}, \text{As}$). The ferromagnetic EuZn_2P_2 shows conspicuous negative magnetoresistance (MR) near T_C , owing to strong magnetic scattering. The MR behavior is consistent with the Majumdar-Littlewood model, indicating that the MR can be enhanced by decreasing the carrier density. Our findings suggest that EuM_2X_2 has highly tunable magnetism and charge transport, making it a promising material family for potential applications in spintronics.

Eu-based layered compounds of EuM_2X_2 ($M = \text{Zn}, \text{Cd}; X = \text{P}, \text{As}, \text{Sb}$) with a trigonal CaAl_2Si_2 -type structure attract great research attention for the successive discoveries of exciting phenomena. EuCd_2As_2 was claimed to be a magnetic Weyl semimetal in the polarized state [1–6], and dramatic alterations in the magnetic ground state and charge transport were observed by applying pressure or changing the crystal growth condition [7–11]. EuCd_2P_2 shows a colossal magnetoresistance (CMR) effect due to the strong magnetic fluctuations well above the Néel temperature (T_N) at 11 K [12], and the onset of ferromagnetic (FM) order was discovered in the temperature range of the strongest CMR [13–15]. The insulator-to-metal transition as well as the topological phase transition was observed for pressurized EuZn_2As_2 [16]. Moreover, CMR effect is also reported for EuZn_2P_2 with semiconducting behavior recently [17].

However, the physical properties reported with samples grown by different recipes are not consistent. For example, the perspective that EuCd_2As_2 is a topological semimetal was challenged by fresh experimental and theoretic evidence, that indicates EuCd_2As_2 is in fact a magnetic semiconductor [18, 19]. In addition, insulating behavior of EuZn_2P_2 was also reported in previous experiments [20, 21]. The varied measurement results suggest the properties of materials in the EuM_2X_2 family are extremely sensitive to carrier concentration, which is usually induced unintentionally by vacancies in the sample.

In this study, we report the successful synthesis of single crystals of EuZn_2P_2 ($T_C = 72$ K), EuZn_2As_2 ($T_C = 42$ K), and EuCd_2P_2 ($T_C = 47$ K) with a FM ground state. Comprehensive characterizations of magnetism and electrical transport for FM- EuZn_2P_2 are presented in the main text. We conclude that the heavy hole doping in FM- EuZn_2P_2 resulting from the Eu vacancies ($\sim 5\%$) is responsible for the interlayer FM coupling, which leads to a transition from an antiferromagnetic (AFM) insulator to the FM metal. We find that these FM- EuM_2X_2 , including FM- EuCd_2As_2 ($T_C = 26$ K) reported before [9], show a linear relationship between the Curie-Weiss temperatures θ_{CW} (as well as T_C) and the Eu-layer distances. This observation not only indicates the prominent role of interlayer Eu-Eu interaction in T_C , but also suggests the probability of T_C promotion by decreasing the layer distance. The switchable magnetic states and charge transport behaviors make EuZn_2P_2 an excellent candidate for future spintronics.

Single crystals of FM- EuZn_2P_2 were grown via a molten salt flux, similar to the growth of FM- EuCd_2As_2 [9]. The details related to the sample growth can be found in the Supplemental Material (SM) [22]. Figure 1 displays the x-ray diffraction (XRD) pattern of FM- EuZn_2P_2 single crystal. Only sharp $(00l)$ diffraction peaks were observed, indicating the high quality of the single crystals. Typically, the crystals grow as millimeter-sized hexagonal thin flakes, as shown in the left inset. The right inset illustrates the structure of EuZn_2P_2 that comprises alternating layers of triangular Eu^{2+} lattice connected by the layer of edge-sharing ZnP_4 tetrahedra. The crystallographic c axis, i.e., the distance of Eu lay-

* wzc@seu.edu.cn

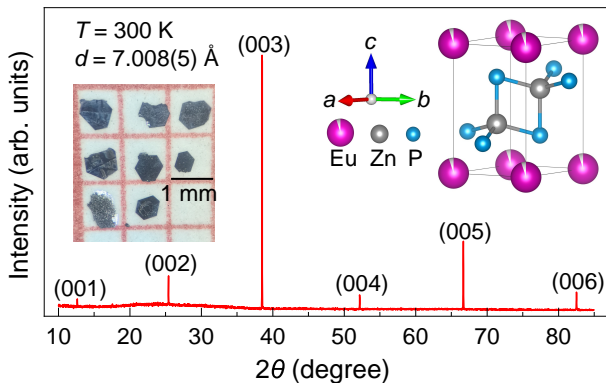


FIG. 1. XRD pattern ($\theta - 2\theta$ scan) of the FM-EuZn₂P₂ single crystal showing only (00 l) reflections. Left inset shows the shape and size of typical FM-EuZn₂P₂ single crystals, and the right inset shows the crystal structure of EuZn₂P₂ with Eu vacancies.

ers, is calculated to be 7.008(5) Å with (00 l) reflections. To further analyze the crystal structure of FM-EuZn₂P₂, the single-crystal XRD (SCXRD) data were collected at $T = 150$ K. The refined result (see Table I) confirms the CaAl₂Si₂-type structure of FM-EuZn₂P₂, and reveals 5% Eu vacancies in the lattice, consistent with a chemical composition resulting from energy dispersive x-ray spectroscopy (EDX, Table S1 in SM) [22]. Compared to the structural parameters reported for AFM-EuZn₂P₂ at 213 K [20], FM-EuZn₂P₂ has a smaller unit cell due to the lower experimental temperature, but its c/a ratio is slightly larger (1.7156 vs. 1.7141 for AFM-EuZn₂P₂), agreeing with the c -axis expansion caused by the hole doping. In a very recent study on AFM-EuZn₂P₂, the interlayer AFM coupling was explained as realized by the superexchange interaction through the Eu-P-P-Eu path [21]. Since the Eu-P and P-P bond lengths as well as the Eu-P-P bond angle are basically unchanged, and no vacancies are found for Zn₂P₂ layers of FM-EuZn₂P₂, it is plausible to assume that the interlayer AFM interaction is kept. Hence, the emerging ferromagnetism should be ascribed to the interlayer FM coupling mediated by the hole carriers. Although the substitution of Na⁺/K⁺ for Eu²⁺ will also result in hole doping, we conclude that the carriers are mainly induced by Eu vacancies, since Na/K is absent from EDX and the heterovalent substitution in EuM₂X₂ seems to be hard in a previous report [23]. In addition, the lattice strain caused by the minor contraction of unit cell ($\sim 0.5\%$) is not likely to be cause of the alterations of properties either, which is evidenced by a recent study about the pressure effect on insulating EuCd₂As₂[24].

The magnetism of FM-EuZn₂P₂ is summarized in Fig. 2. A clear hysteresis loop can be found for the $M(H)$ curve with the in-plane field ($H \parallel ab$) at 1.8 K, shown in panel (a). And the hysteresis loop with the out-of-plane field is indistinctive ($H \parallel c$) compared to the in-plane curve, suggesting that the spins should be aligned

TABLE I. Crystallographic data and refinement result of FM-EuZn₂P₂ from the SCXRD at 150 K [25]. The occupancies of Zn and P were fixed to 1.0 to avoid unphysical values greater than 1.

Material	FM-EuZn ₂ P ₂
Crystal system	Trigonal
Space group	$P\bar{3}m1$ (No. 164)
a (Å)	4.0765(2)
c (Å)	6.9936(4)
c/a	1.7156
V (Å ³)	100.648(11)
Z	1
Eu site occupancy	0.950(8)
Temperature (K)	150
Radiation	Mo $K\alpha$
Reflections collected	1424
Independent reflections	104
R_{int}	0.0819
Goodness-of-fit	1.345
R_1^a	0.0339
wR_2^b	0.0984
Fractional coordinates	
Eu	(0,0,0)
Zn	(1/3,2/3,0.6305(4))
P	(1/3,2/3,0.2691(7))

^a $R_1 = \Sigma ||F_o| - |F_c|| / \Sigma |F_o|$.

^b $wR_2 = [\Sigma w(F_o^2 - F_c^2)^2 / \Sigma w(F_o^2)]^{1/2}$.

in the ab plane, as illustrated by the inset. Recent studies have demonstrated that the magnetic ordering of AFM-EuZn₂P₂ is A type, i.e. in-plane FM coupling and out-of-plane AFM coupling, whose $M(H)$ curves do not exhibit any hysteresis [17, 20, 21]. The significant difference in $M(H)$ curves between AFM- and FM-EuZn₂P₂ indicates that the intrinsic FM-EuZn₂P₂ is successfully prepared by changing the growth condition.

Figure 2(b) displays the comparison of $M(H)$ curves between FM- and AFM-EuZn₂P₂. For FM-EuZn₂P₂, the $M(H)$ curves exhibit strong magnetocrystalline anisotropy. The saturation field (H_{sat}) for the in-plane magnetization is only about 0.1 T, while the out-of-plane magnetization increases rapidly below 0.1 T and finally saturates at the field over 2.5 T. The similar metamagnetic transition around 0.1 T with the c -axis field was also reported for FM-EuCd₂As₂, which was attributed to the increasing canting of spins in the external field [10]. The large magnetocrystalline anisotropy (over 25 times on the basis of H_{sat}) suggests that the Eu layer (the ab plane) is the magnetic easy plane. We notice that the values of H_{sat} ($H \parallel c$) for FM- and AFM-EuZn₂P₂ are comparable, while H_{sat} of FM-EuCd₂As₂ for $H \parallel ab$ is noticeably reduced. The conspicuous change in H_{sat} manifests that the FM coupling between the Eu layers is much enhanced by the induced carries. In addition, the saturated mag-

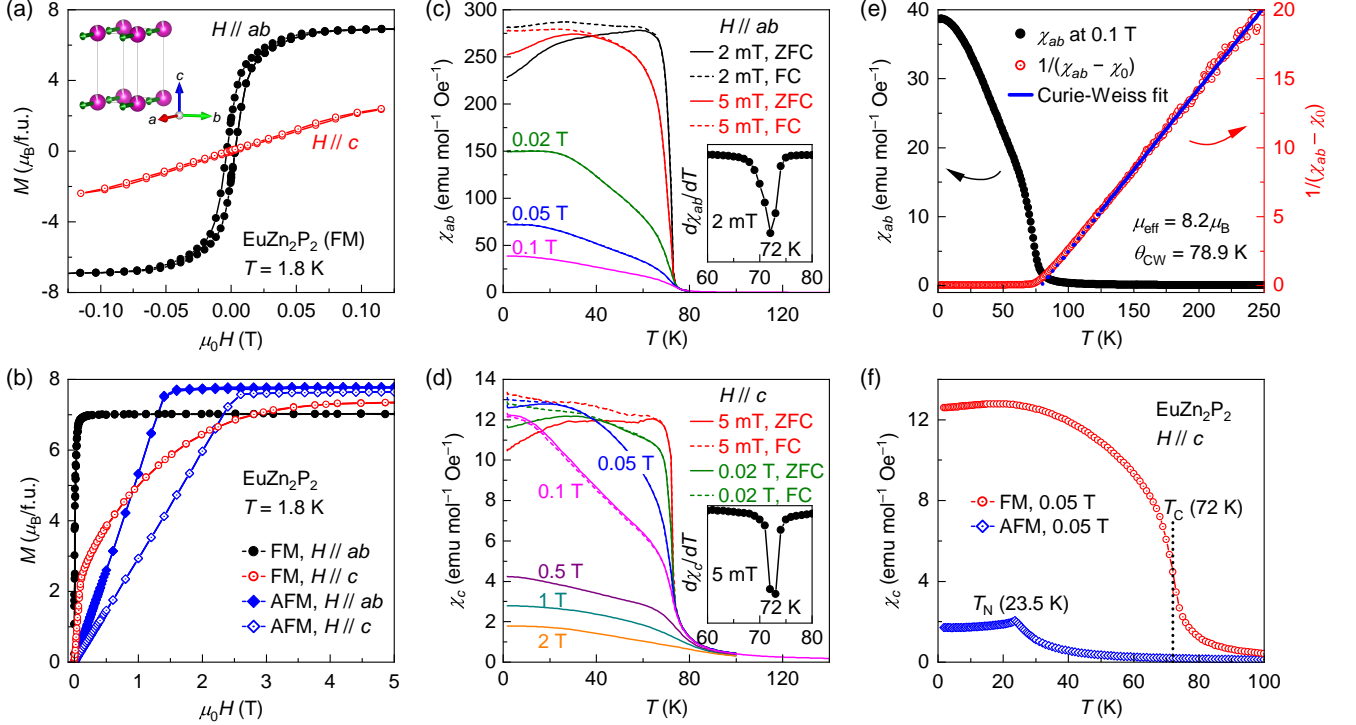


FIG. 2. (a) Magnetic hysteresis loops of FM-EuZn₂P₂ at 1.8 K for fields in the *ab* plane (black) and along the *c* axis (red). Inset shows the spin configuration of FM-EuZn₂P₂. (b) Magnetization as a function of field for FM- (black and red circles) and AFM- (blue diamonds) EuZn₂P₂ at $T = 1.8$ K. [(c), (d)] Temperature dependences of magnetic susceptibility for field parallel to the *ab* plane (c) and the *c* axis (d). Their insets present the derivative of the magnetic susceptibility ($d\chi/dT$) to show the transition temperatures. (e) Curie-Weiss analysis from 125 to 300 K with $\chi_{ab}(T)$ data at 0.1 T. Only data below 250 K are shown. (f) The magnetic transitions for FM- (red) and AFM-EuZn₂P₂ (blue) at 0.05 T.

netizations (M_{sat}) of FM-EuZn₂P₂ reach about $7\mu_{\text{B}}$ for both directions at 1.8 K, consistent with the Eu²⁺ oxidation state.

Figures 2(c) and 2(d) show the curves of temperature-dependent magnetic susceptibility of FM-EuZn₂P₂ under the in-plane and out-of-plane magnetic fields, respectively. Both $\chi_{ab}(T)$ and $\chi_c(T)$ increase dramatically below 80 K, and evident bifurcations of zero-field-cooling (ZFC) and field-cooling (FC) data are observed with small fields, which is the typical feature for ferromagnets and is consistent with the hysteresis loops in Fig. 2(a). The splittings are rapidly suppressed with the increasing field. The Curie temperature (T_{C}) of FM-EuZn₂P₂ is determined by the susceptibility derivatives ($d\chi/dT$), shown in the insets of Figs. 2(c) and 2(d). T_{C} is identified to be 72 K by both $d\chi_{ab}/dT$ and $d\chi_c/dT$. Moreover, we notice that χ_{ab} is about an order of magnitude larger than χ_c for the small fields, which confirms the strong magnetocrystalline anisotropy of FM-EuZn₂P₂ in Figs. 2(a) and 2(b).

The Curie-Weiss analysis of $\chi_{ab}(T)$ is presented in Fig. 2(e). The data above 125 K is fitted with $\chi_{ab} = \chi_0 + C/(T - \theta_{\text{CW}})$, which yields $C = 8.47$ emu K mol⁻¹ Oe⁻¹ (effective moment $\mu_{\text{eff}} = 8.2\mu_{\text{B}}$ /f.u.), $\theta_{\text{CW}} = 78.9$ K, and $\chi_0 = 1.39 \times 10^{-4}$ emu mol⁻¹ Oe⁻¹. The value of μ_{eff} is coincident with the theoretical value of $7.94\mu_{\text{B}}$

for Eu²⁺. The Curie-Weiss temperature θ_{CW} is close to the experimentally determined T_{C} , indicating that EuZn₂P₂ is manipulated to be an intrinsic ferromagnet rather than a canted antiferromagnet. $\chi_c(T)$ of AFM- and FM-EuZn₂P₂ are compared in Fig. 2(f). AFM-EuZn₂P₂ exhibits a conspicuous peak at 23.5 K, agreeing well with the reported Néel temperature (T_{N}) [17, 20, 21]. The distinct behaviors of $\chi_c(T)$ confirm the alteration of ground-state and the dominant FM interaction in FM-EuZn₂P₂. T_{C} of FM-EuZn₂P₂ is significantly higher than those of the sister materials with a FM state (47 K for EuCd₂P₂, 26 K for EuCd₂As₂, 42 K for EuZn₂As₂, see SM) [22], which is attributed to its smaller distance of Eu layers and is discussed later.

FM-EuZn₂P₂ exhibits a metallic behavior, as shown in Fig. 3(a). In the paramagnetic (PM) region (above 120 K), the zero-field in-plane resistivity (ρ_{ab}) decreases as the temperature goes down, and then shows a mild rise in the region of magnetic fluctuation ($T_{\text{C}} \lesssim T \lesssim 1.5T_{\text{C}}$) due to the enhanced scattering. Finally, ρ_{ab} decreases monotonically below the FM ordering at 72 K. The residual resistivity ratio (RRR, a ratio of $R_{300\text{K}}$ and $R_{0\text{K}}$) is 6, and remains almost unchanged in the field. Considering 5% Eu²⁺ vacancies in the lattice, the hole concentration in FM-EuZn₂P₂ is estimated to be 10^{21} cm⁻³ based on the single-band model, which results in the Mott-Ioffe-

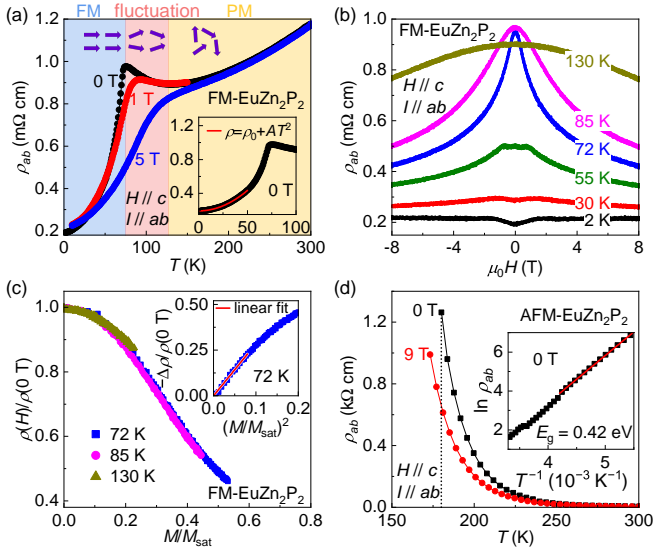


FIG. 3. (a) In-plane resistivity of FM-EuZn₂P₂ as a function temperature under several fields. Inset shows a fit (red curve) with the parabolic function $\rho(T) = \rho_0 + AT^2$ to the zero-field resistivity below 50 K. (b) Field-dependent resistivity of FM-EuZn₂P₂ at various temperatures from 2 to 130 K. (c) Normalized resistivity $\rho(H)/\rho(0\text{ T})$ at 72 K (blue squares), 85 K (magenta circles), and 130 K (dark yellow triangles) plotted against normalized field-induced magnetization M/M_{sat} , where M_{sat} is the saturated magnetization, i.e., $7\mu_B$. Inset plots $-\text{MR}$ as a function of $(M/M_{\text{sat}})^2$ and a linear fit (red line) for $(M/M_{\text{sat}})^2 \leq 0.08$. (d) In-plane resistivity of AFM-EuZn₂P₂ at 0 and 9 T. Inset displays the Arrhenius plot ($\ln \rho_{ab}$ vs T^{-1}) of zero-field data, as well as a linear fit (red line).

Regel (MIR) limit of 0.7 mΩ cm [26]. Since the residual resistivity at 2 K (~ 0.2 mΩ cm) is below the MIR limit, FM-EuZn₂P₂ is a good metal with a relatively long mean free path. We found that the behavior of zero-field $\rho_{ab}(T)$ below 50 K could be well described with a simple quadratic function $\rho(T) = \rho_0 + AT^2$, where the T^2 dependence is contributed by the electron-electron or electron-magnon scattering. The resultant fitting parameters are $\rho_0 = 0.193$ mΩ cm, $A = 9.60 \times 10^{-5}$ mΩ cm K⁻². The typical Fermi liquid behavior indicates the negligible electron-phonon scattering at low temperatures and the weak electron correlation of FM-EuZn₂P₂.

The resistivity peak at T_C is suppressed by applying the external magnetic fields. The curves of ρ_{ab} as a function of field are plotted in Fig. 3(b). The maximum negative magnetoresistance (MR) is achieved at T_C , which is over -50% at 8 T with the definition $\text{MR} = 100\% \times [\rho(H) - \rho(0)]/\rho(0)$. For the temperatures well below T_C , the negative MR is weak and a small enhancement in $\rho_{ab}(H)$ is observed when the field is low, which is also seen for FM-EuCd₂As₂ and should be related to the increased canting of spins towards the c axis in the field [10]. The normalized resistivity $\rho(H)/\rho(0\text{ T})$ at 72 K (T_C), 85 K ($1.2T_C$), and 130 K ($1.8T_C$) against normal-

ized magnetization (M/M_{sat}) is plotted in Fig. 3(c). The resistivity at three different temperatures change with magnetization by following a similar trace. The good correlation implies that the MR of FM-EuZn₂P₂ is closely related to the magnetization, which means that magnetic scattering plays a major role in the MR of FM-EuZn₂P₂. In the inset of Fig. 3(c), we plot $-\text{MR}$ at 72 K, i.e., $-\Delta\rho/\rho(0\text{ T})$, as a function of $(M/M_{\text{sat}})^2$. It is seen that the magnitude of $-\text{MR}$ obeys the scaling function

$$-\Delta\rho/\rho(0\text{ T}) = C_{\text{MR}}(M/M_{\text{sat}})^2, \quad (1)$$

in the relatively low- M region, say $M/M_{\text{sat}} \leq 0.3$. The scaling factor C_{MR} is 2.85, resulting from the linear fit with the data in low- M region. Since the metallic transport of FM-EuZn₂P₂, the Majumdar-Littlewood model is applicable to elucidate the dependence of MR on charge-carrier density [27]. According to the model, C_{MR} could be estimated with the relation $C_{\text{MR}} \approx x^{-2/3}$, where x is the number of charge carriers per magnetic unit cell. In the case of FM-EuZn₂P₂, $x \approx 0.1$ due to 5% Eu²⁺ vacancies. Then we have $C_{\text{MR}} = 4.6$, comparable to the fitting value. Hence, the enhanced MR effect of FM-EuZn₂P₂ is expected by simply declining the carrier concentration, which could be realized through chemical doping or electrostatic gating.

We also measured the in-plane resistivity of AFM-EuZn₂P₂ for comparison, which is three orders of magnitude higher than that of FM-EuZn₂P₂ at 300 K, as shown in Fig. 3(d). AFM-EuZn₂P₂ is insulating without the magnetic field. By applying a field of 9 T, ρ_{ab} declines by half at 180 K yet the insulating behavior is retained. The band gap is estimated to be 0.42 eV with the Arrhenius model $\rho \propto e^{E_g/2k_B T}$, consistent with earlier studies [20, 21]. The distinct charge-transport behaviors of FM- and AFM-EuZn₂P₂ demonstrate that this system is successfully tuned from an AFM insulator into a FM metal by inducing the carriers.

To get a deeper understanding of the carrier-induced ferromagnetism in EuM₂X₂ ($M = \text{Zn, Cd}$; $X = \text{P, As}$), we synthesized FM-EuZn₂As₂ ($T_C = 42$ K) and FM-EuCd₂P₂ ($T_C = 47$ K) via the salt flux method as well. The characterizations of magnetism are presented in Figs. S3 and S4 in the SM [22]. The characteristic temperatures (T_C , T_N , θ_{CW}) of both FM- and AFM-EuM₂X₂ are plotted as a function of the Eu-layer distance (d_{inter}) in Fig. 4. Note that since the structural difference between EuM₂X₂ with the FM and AFM states is pretty small, we use the c -axis value reported for AFM-EuM₂X₂ at room temperature as d_{inter} for both materials [9, 12, 20, 28]. T_N and θ_{CW} of AFM-EuM₂X₂ do not show a monotonic dependence on d_{inter} , while T_C and θ_{CW} of FM-EuM₂X₂ increase almost linearly with decreasing d_{inter} . These linear relationships convincingly demonstrate that the FM ordering temperatures of FM-EuM₂X₂ mainly depend on the interlayer Eu-Eu coupling. Thus T_C could be further enhanced by applying pressure or doping smaller divalent ions such as Ca²⁺ to decrease the layer distance. Actually, T_C over 100 K was

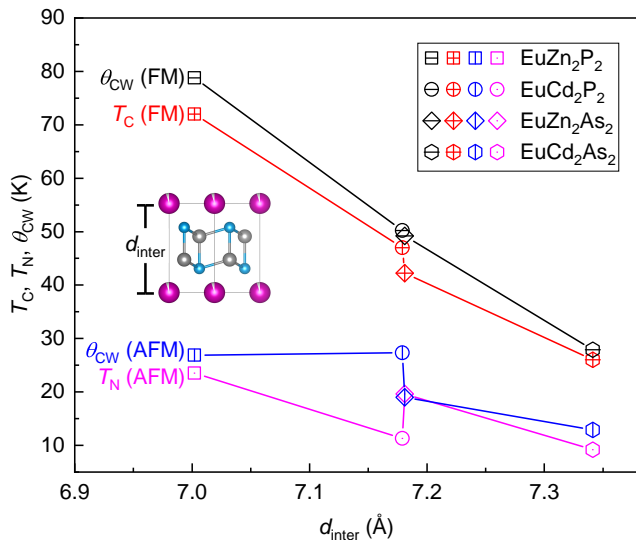


FIG. 4. The characteristic temperatures (T_{C} , T_{N} , θ_{CW}) of EuM_2X_2 ($M = \text{Zn}, \text{Cd}$; $X = \text{P}, \text{As}$) as a function of the Eu-layer distance, i.e., the c axis. The squares, circles, diamonds, and hexagons represent the data of EuZn_2P_2 , EuCd_2P_2 , EuZn_2As_2 , and EuCd_2As_2 , respectively. The error bars are not shown because the uncertainties of data points are smaller than the size of symbols.

reported in pressurized EuZn_2As_2 [16]. We notice that all values of T_{C} are slightly smaller than the corresponding θ_{CW} , which is ascribed to the influence of existing interlayer AFM interaction through the Eu- X - X -Eu superexchange path, as mentioned earlier [21]. Therefore, it is natural to see a larger discrepancy between T_{C} and θ_{CW} for FM- EuZn_2P_2 and FM- EuZn_2As_2 due to their shorter Eu- X - X -Eu path.

Our results manifest that the interlayer FM coupling is essential to the FM ordering temperature, and the FM interaction results from the indirect exchange mediated by carriers. The role of carrier densities has not been discussed yet. It seems that the influence of carrier concentration on T_{C} is not primary in the case of EuM_2X_2 . For example, T_{C} and θ_{CW} of FM- EuCd_2As_2 vary only several kelvins when the chemical doping level changes by an order of magnitude [23]. Since the carrier concentrations of FM- EuM_2X_2 are lower than the validity condition of the Ruderman-Kittel-Kasuya-Yosida (RKKY) theory ($> 10^{21} \text{ cm}^{-3}$), the dependence of interlayer FM

interaction on the carrier density cannot be understood within this framework [29]. Nevertheless, the correlation between T_{C} and carrier density is not ruled out. Further theoretic and experimental efforts will be devoted to investigating the effect of carrier density on T_{C} .

In summary, FM- EuZn_2P_2 was successfully grown via the salt flux method, which has similar structural parameters to AFM- EuZn_2P_2 except for 5% Eu vacancies. The magnetization and resistivity measurements show that the defective EuZn_2P_2 is a FM metal of $T_{\text{C}} = 72 \text{ K}$, rather than an AFM insulator of $T_{\text{N}} = 23.5 \text{ K}$, as in the vacancy-free version. The analysis of field-dependent resistivity indicates that the magnetic scattering makes the main contribution to the resistivity near T_{C} . On basis of the Majumdar-Littlewood model, a greater MR effect is probably achieved by reducing the carrier density. The transition temperatures and Curie-Weiss temperatures of AFM- and FM- EuM_2X_2 ($M = \text{Zn}, \text{Cd}$; $X = \text{P}, \text{As}$) are examined, which reveals linear dependences of θ_{CW} and T_{C} on the Eu-layer distance, indicating the critical role of interlayer FM coupling on the FM ordering. Our results suggest that FM coupling could be induced with low carrier densities in Eu-based CaAl_2Si_2 -type materials, which may also be applicable to other AFM Eu-based Zintl compounds such as EuIn_2As_2 and EuMn_2P_2 , for their narrow energy gaps and similar layered structures. Moreover, it is of great interest to explore other exotic phenomena such as the topological phase transition by tuning the carrier concentration of EuM_2X_2 in controlled manners like chemical doping and the gating technique, which is not only important for fundamental research, but also significant for potential applications in spintronics.

ACKNOWLEDGMENTS

This work was supported by the National Natural Science Foundation of China (Grants No. 12204094), the Natural Science Foundation of Jiangsu Province (Grant No. BK20220796), the Start-up Research Fund of Southeast University (Grant No. RF1028623289), the Interdisciplinary program of Wuhan National High Magnetic Field Center (WHMFC) at Huazhong University of Science and Technology (Grant No. WHMFC202205), and the open research fund of Key Laboratory of Quantum Materials and Devices (Southeast University), Ministry of Education.

- [1] G. Hua, S. Nie, Z. Song, R. Yu, G. Xu, and K. Yao, Dirac semimetal in type-IV magnetic space groups, *Phys. Rev. B* **98**, 201116(R) (2018).
- [2] J.-R. Soh, F. de Juan, M. G. Vergniory, N. B. M. Schröter, M. C. Rahn, D. Y. Yan, J. Jiang, M. Bristow, P. Reiss, J. N. Blandy, Y. F. Guo, Y. G. Shi, T. K. Kim, A. McCollam, S. H. Simon, Y. Chen, A. I. Coldea,

and A. T. Boothroyd, Ideal Weyl semimetal induced by magnetic exchange, *Phys. Rev. B* **100**, 201102(R) (2019).

- [3] L.-L. Wang, N. H. Jo, B. Kuthanazhi, Y. Wu, R. J. McQueeney, A. Kaminski, and P. C. Canfield, Single pair of weyl fermions in the half-metallic semimetal EuCd_2As_2 , *Phys. Rev. B* **99**, 245147 (2019).
- [4] M. C. Rahn, J.-R. Soh, S. Francoual, L. S. I. Veiga,

- J. Stremper, J. Mardegan, D. Y. Yan, Y. F. Guo, Y. G. Shi, and A. T. Boothroyd, Coupling of magnetic order and charge transport in the candidate Dirac semimetal EuCd_2As_2 , *Phys. Rev. B* **97**, 214422 (2018).
- [5] J.-Z. Ma, S. M. Nie, C. J. Yi, J. Jandke, T. Shang, M. Y. Yao, M. Naamneh, L. Q. Yan, Y. Sun, A. Chikina, V. N. Strocov, M. Medarde, M. Song, Y.-M. Xiong, G. Xu, W. Wulfhchel, J. Mesot, M. Reticcioli, C. Franchini, C. Mudry, M. Müller, Y. G. Shi, T. Qian, H. Ding, and M. Shi, Spin fluctuation induced Weyl semimetal state in the paramagnetic phase of EuCd_2As_2 , *Sci. Adv.* **5**, eaaw4718 (2019).
- [6] Y. Xu, L. Das, J. Z. Ma, C. J. Yi, S. M. Nie, Y. G. Shi, A. Tiwari, S. S. Tsirkin, T. Neupert, M. Medarde, M. Shi, J. Chang, and T. Shang, Unconventional Transverse Transport above and below the Magnetic Transition Temperature in Weyl Semimetal EuCd_2As_2 , *Phys. Rev. Lett.* **126**, 076602 (2021).
- [7] E. Gati, S. L. Bud'ko, L.-L. Wang, A. Valadkhan, R. Gupta, B. Kuthanazhi, L. Xiang, J. M. Wilde, A. Sapkota, Z. Guguchia, R. Khasanov, R. Valentí, and P. C. Canfield, Pressure-induced ferromagnetism in the topological semimetal EuCd_2As_2 , *Phys. Rev. B* **104**, 155124 (2021).
- [8] F. Du, L. Yang, Z. Nie, N. Wu, Y. Li, S. Luo, Y. Chen, D. Su, M. Smidman, Y. Shi, C. Cao, F. Steglich, Y. Song, and H. Yuan, Consecutive topological phase transitions and colossal magnetoresistance in a magnetic topological semimetal, *npj Quantum Mater.* **7**, 65 (2022).
- [9] N. H. Jo, B. Kuthanazhi, Y. Wu, E. Timmons, T.-H. Kim, L. Zhou, L.-L. Wang, B. G. Ueland, A. Palasyuk, D. H. Ryan, R. J. McQueeney, K. Lee, B. Schruck, A. A. Burkov, R. Prozorov, S. L. Bud'ko, A. Kaminski, and P. C. Canfield, Manipulating magnetism in the topological semimetal EuCd_2As_2 , *Phys. Rev. B* **101**, 140402(R) (2020).
- [10] S. Roychowdhury, M. Yao, K. Samanta, S. Bae, D. Chen, S. Ju, A. Raghavan, N. Kumar, P. Constantinou, S. N. Guin, N. C. Plumb, M. Romanelli, H. Borrmann, M. G. Vergniory, V. N. Strocov, V. Madhavan, C. Shekhar, and C. Felser, Anomalous Hall Conductivity and Nernst Effect of the Ideal Weyl Semimetallic Ferromagnet EuCd_2As_2 , *Adv. Sci.* **10**, 2207121 (2023).
- [11] K. M. Taddei, L. Yin, L. D. Sanjeewa, Y. Li, J. Xing, C. dela Cruz, D. Phelan, A. S. Sefat, and D. S. Parker, Single pair of Weyl nodes in the spin-canted structure of EuCd_2As_2 , *Phys. Rev. B* **105**, L140401 (2022).
- [12] Z.-C. Wang, J. D. Rogers, X. Yao, R. Nichols, K. Atay, B. Xu, J. Franklin, I. Sochnikov, P. J. Ryan, D. Haskel, and F. Tafti, Colossal Magnetoresistance without Mixed Valence in a Layered Phosphide Crystal, *Adv. Mater.* **33**, 2005755 (2021).
- [13] V. Sunko, Y. Sun, M. Vranas, C. C. Homes, C. Lee, E. Donoway, Z.-C. Wang, S. Balguri, M. B. Mahendru, A. Ruiz, B. Gunn, R. Basak, S. Blanco-Canosa, E. Schierle, E. Weschke, F. Tafti, A. Frano, and J. Orenstein, Spin-carrier coupling induced ferromagnetism and giant resistivity peak in EuCd_2P_2 , *Phys. Rev. B* **107**, 144404 (2023).
- [14] C. C. Homes, Z.-C. Wang, K. Fruhling, and F. Tafti, Optical properties and carrier localization in the layered phosphide EuCd_2P_2 , *Phys. Rev. B* **107**, 045106 (2023).
- [15] H. Zhang, F. Du, X. Zheng, S. Luo, Y. Wu, H. Zheng, S. Cui, Z. Sun, Z. Liu, D. Shen, M. Smidman, Y. Song, M. Shi, Z. Zhong, C. Cao, H. Yuan, and Y. Liu, Electronic band reconstruction across the insulator-metal transition in colossally magnetoresistive EuCd_2P_2 , *Phys. Rev. B* **108**, L241115 (2023).
- [16] S. Luo, Y. Xu, F. Du, L. Yang, Y. Chen, C. Cao, Y. Song, and H. Yuan, Colossal magnetoresistance and topological phase transition in EuZn_2As_2 , *Phys. Rev. B* **108**, 205140 (2023).
- [17] S. Kriebber, M. Kopp, C. Garg, K. Kummer, J. Sichelschmidt, S. Schulz, G. Poelchen, M. Mende, A. V. Virovets, K. Warawa, M. D. Thomson, A. V. Tarasov, D. Y. Usachov, D. V. Vyalikh, H. G. Roskos, J. Müller, C. Krellner, and K. Kliemt, Colossal magnetoresistance in EuZn_2P_2 and its electronic and magnetic structure, *Phys. Rev. B* **108**, 045116 (2023).
- [18] D. Santos-Cottin, I. Mohelský, J. Wyzula, F. Le Mardelé, I. Kapon, S. Nasrallah, N. Barišić, I. Živković, J. R. Soh, F. Guo, K. Rigaux, M. Puppini, J. H. Dil, B. Gudac, Z. Rukelj, M. Novak, A. B. Kuzmenko, C. C. Homes, T. Dietl, M. Orlita, and A. Akrap, EuCd_2As_2 : A Magnetic Semiconductor, *Phys. Rev. Lett.* **131**, 186704 (2023).
- [19] Y. Shi, Z. Liu, L. A. Burnett, S. Lee, C. Hu, Q. Jiang, J. Cai, X. Xu, C.-C. Chen, and J.-H. Chu, Absence of Weyl nodes in EuCd_2As_2 revealed by the carrier density dependence of the anomalous Hall effect (2023), arxiv:2401.00138 [cond-mat].
- [20] T. Berry, V. J. Stewart, B. W. Y. Redemann, C. Lygouras, N. Varnava, D. Vanderbilt, and T. M. McQueen, A-type antiferromagnetic order in the Zintl-phase insulator EuZn_2P_2 , *Phys. Rev. B* **106**, 054420 (2022).
- [21] K. Singh, S. Dan, A. Ptok, T. A. Zaleski, O. Pavloviuk, P. Wiśniewski, and D. Kaczorowski, Superexchange interaction in insulating EuZn_2P_2 , *Phys. Rev. B* **108**, 054402 (2023).
- [22] See the Supplemental Material for experimental details, chemical composition analysis of FM- EuZn_2P_2 , AFM- EuZn_2P_2 and FM- EuZn_2As_2 , structural analysis of AFM- EuZn_2P_2 , supporting data for magnetism of EuZn_2P_2 , FM- EuZn_2As_2 , and FM- EuCd_2P_2 .
- [23] B. Kuthanazhi, K. R. Joshi, S. Ghimire, E. Timmons, L.-L. Wang, E. Gati, L. Xiang, R. Prozorov, S. L. Bud'ko, and P. C. Canfield, Magnetism and T - x phase diagrams of Na- and Ag-substituted EuCd_2As_2 , *Phys. Rev. Materials* **7**, 034402 (2023).
- [24] X. Chen, S. Wang, J. Wang, C. An, Y. Zhou, Z. Chen, X. Zhu, Y. Zhou, Z. Yang, and M. Tian, Temperature-pressure phase diagram of the intrinsically insulating topological antiferromagnet EuCd_2As_2 , *Phys. Rev. B* **107**, L241106 (2023).
- [25] CCDC 2330806 contains the supplementary crystallographic data for FM- EuZn_2P_2 .
- [26] M. Gurvitch, Ioffe-Regel criterion and resistivity of metals, *Phys. Rev. B* **24**, 7404 (1981).
- [27] P. Majumdar and P. B. Littlewood, Dependence of magnetoresistivity on charge-carrier density in metallic ferromagnets and doped magnetic semiconductors, *Nature* **395**, 479 (1998).
- [28] Z.-C. Wang, E. Been, J. Gaudet, G. Alqasseri, K. Fruhling, X. Yao, U. Stuhr, Q. Zhu, Z. Ren, Y. Cui, C. Jia, B. Moritz, S. Chowdhury, T. Devereaux, and F. Tafti, Anisotropy of the magnetic and transport properties of EuZn_2As_2 , *Phys. Rev. B* **105**, 165122 (2022).

- [29] É. Nagaev, Indirect exchange in ferromagnets with low carrier densities, *Zh. Eksp. Teor. Fiz.* **90**, 652 (1986).

**Supplemental Materials: Carrier-induced transition from
antiferromagnetic insulator to ferromagnetic metal in the layered
phosphide EuZn_2P_2**

Xiyu Chen,¹ Wuzhang Yang,^{2,3} Jia-Yi Lu,⁴ Zhiyu Zhou,¹ Zhi
Ren,^{2,3} Guang-Han Cao,^{4,5} Shuai Dong,¹ and Zhi-Cheng Wang^{1,*}

¹*Key Laboratory of Quantum Materials and Devices of Ministry of Education,
School of Physics, Southeast University, Nanjing 211189, China*

²*School of Science, Westlake University, Hangzhou 310024, China*

³*Institute of Natural Sciences, Westlake Institute
for Advanced Study, Hangzhou 310024, China*

⁴*School of Physics, Interdisciplinary Center for Quantum Information and
State Key Laboratory of Silicon and Advanced Semiconductor Materials,
Zhejiang University, Hangzhou 310058, China*

⁵*Collaborative Innovation Centre of Advanced Microstructures,
Nanjing University, Nanjing 210093, China*

(Dated: June 11, 2024)

Content

- A:** Experimental methods for the crystal growth and characterizations.
- B:** Figure S1 and Table S1. Chemical composition analysis of FM-EuZn₂P₂ via energy dispersive spectroscopy.
- C:** Figure S2 and Table S2. Chemical composition analysis of AFM-EuZn₂P₂ via energy dispersive spectroscopy.
- D:** Figure S3 and Table S3. X-ray diffraction pattern and the Rietveld refinement of AFM-EuZn₂P₂
- E:** Figure S4 and S5. Magnetic data of FM- and AFM-EuZn₂P₂
- F:** Figure S6. Magnetism of FM-EuZn₂As₂
- G:** Figure S7. Magnetism of FM-EuCd₂P₂
- H:** Figure S8. SEM images and chemical composition of FM-EuZn₂As₂

* wzc@seu.edu.cn

A. Methods

Crystal growth. The Eu ingots (99.999%), Zn powder (99.99%), red P lumps (99.999%), As powder (99.99%), Sn shots (99.99%), NaCl (99.99%), and KCl (99.99%) were used to grow single crystals of EuZn_2P_2 and EuZn_2As_2 . FM- EuZn_2P_2 single crystals were grown with salt flux of an equimolar mixture of NaCl/KCl. A total mass of 1 g of Eu, Zn, and P was weighed using a molar ratio of 1:2:2. The reactants were mixed with 4 g of the salt flux, then placed in a quartz tube, which was sealed under high vacuum ($< 10^{-2}$ Pa). Next, the firstly sealed quartz tube was loaded into a second quartz tube with slightly larger diameter, which was also vacuumed and sealed. The nested tubes were heated to 469 °C over 24 h, held for 24 h, then heated to 597 °C in a rate of 20 °C/h and held for another 24 h. Afterwards, the tubes were heated to 847 °C and held for 50 h, and subsequently cooled to 630 °C at 1.5 °C/h. Shiny flakes of crystals can be obtained by washing the product with deionized water. FM- EuZn_2As_2 and FM- EuCd_2P_2 single crystals were grown through a similar method like FM- EuZn_2P_2 . The scanning electron microscopy (SEM) micrographs of FM- EuZn_2As_2 are shown in Fig. S8, which are brittle and not good enough for the measurements of transport properties. AFM- EuZn_2P_2 was grown by Sn flux. The elements were mixed in a molar ratio $\text{Eu}:\text{Zn}:\text{P}:\text{Sn} = 1:1:1:8$. The mixture was loaded into an alumina crucible inside an evacuated quartz ampule and slowly heated to 1100 °C, held for 24 h, cooled to 900 °C at 3 °C/h, cooled to 600 °C at 5 °C/h, and finally centrifuged to remove the flux.

Structure Determination and Chemical Compositions Characterization. The PANalytical x-ray diffractometer with the Cu $K\alpha_1$ radiation was used to check the quality of single crystals at room temperature. The crystal structure of FM- EuZn_2P_2 at 150 K was determined by a Bruker D8 Venture diffractometer equipped with I μ S 3.0 Dual Wavelength system (Mo $K\alpha$ radiation, $\lambda = 0.71073$ Å), and an APEX-II CCD detector. The initial structural model was developed with the intrinsic phasing feature of SHELXT and a least-square refinement was performed using SHELXL2014. The chemical compositions of single crystals were characterized by scanning electron microscopy (FEI Inspect F50) with Amatek EDAX EDS detector.

Magnetization and Transport Measurements. The direct-current (dc) magnetization was measured using a magnetic property measurement system (MPMS-3, Quantum Design). The resistivity was collected with a standard four-probe technique using a physical property

measurement system (PPMS-9, Quantum Design).

B. Chemical composition analysis of FM-EuZn₂P₂

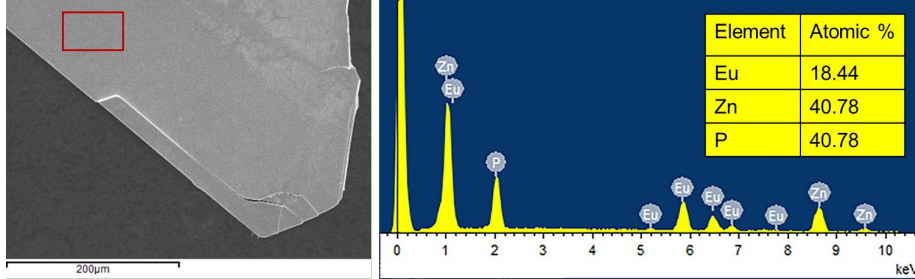


FIG. S1. A typical energy dispersive x-ray spectrum of FM-EuZn₂P₂ single crystal.

TABLE S1. Chemical composition analysis of FM-EuZn₂P₂ single crystals via energy dispersive x-ray spectroscopy. The number of Zn atoms in a formula unit is normalized to 2, and other data are rescaled accordingly. The first column shows the data points and corresponding specimens, for example, "S1, P1" represents the first point from sample 1, and so on. The resulting chemical formula is Eu_{0.96(3)}Zn_{2.00}P_{2.11(6)}.

	Eu	Zn	P	Eu/P
S1, P1	0.93	2.00	2.15	0.43
S1, P2	1.00	2.00	2.22	0.45
S2, P1	0.93	2.00	2.11	0.44
S2, P2	0.94	2.00	2.05	0.46
S2, P3	0.90	2.00	2.00	0.45
S3, P1	0.96	2.00	2.07	0.46
S3, P2	0.97	2.00	2.13	0.45
S4, P1	0.99	2.00	2.13	0.46
S4, P2	0.99	2.00	2.08	0.48
S4, P3	1.00	2.00	2.11	0.47
average	0.96	2.00	2.11	0.46
stand deviation	0.03	0.00	0.06	0.013

C. Chemical composition analysis of AFM-EuZn₂P₂

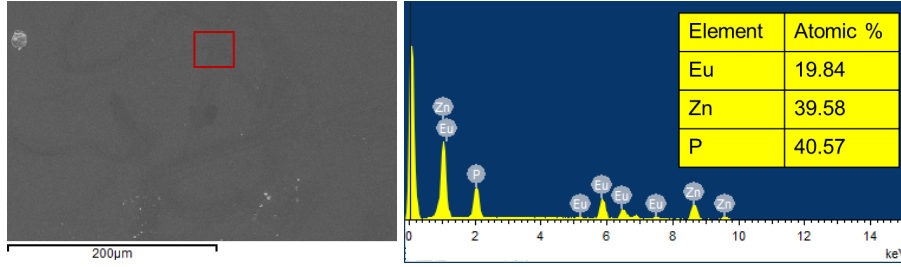


FIG. S2. A typical energy dispersive x-ray spectrum of AFM-EuZn₂P₂ single crystal.

TABLE S2. Chemical composition analysis of AFM-EuZn₂P₂ single crystals via energy dispersive x-ray spectroscopy. The number of Zn atoms in a formula unit is normalized to 2, and other data are rescaled accordingly. The resulting chemical formula is Eu_{0.99(2)}Zn_{2.00}P_{1.98(13)}.

	Eu	Zn	P	Eu/P
S1, P1	1.00	2.00	2.05	0.49
S1, P2	1.02	2.00	2.13	0.48
S1, P3	1.00	2.00	2.13	0.47
S1, P4	1.01	2.00	2.11	0.48
S2, P1	0.96	2.00	1.89	0.51
S2, P2	0.97	2.00	1.85	0.52
S2, P3	0.98	2.00	1.84	0.53
S2, P4	0.99	2.00	1.88	0.53
average	0.99	2.00	1.98	0.50
stand deviation	0.02	0.00	0.13	0.03

D. Structural analysis of AFM-EuZn₂P₂

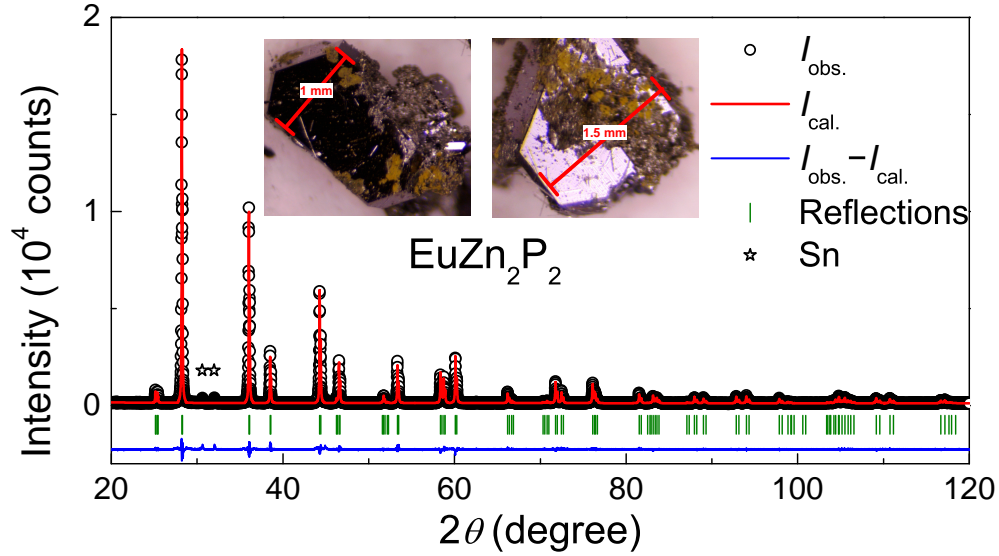


FIG. S3. X-ray diffraction pattern and the Rietveld refinement of AFM-EuZn₂P₂, collected at room temperature by grinding the single crystals into powder.

TABLE S3. Unit cell dimensions and refinement parameters are listed for AFM-EuZn₂P₂ from the Rietveld refinements in the space group $P\bar{3}m1$. The atomic coordinates are as follows: Eu 1a (0,0,0); Zn 2d (1/3,2/3,0.6310(2)); P 2d (1/3,2/3,0.2706(4)). All sites are fully occupied.

Material	AFM-EuZn ₂ P ₂
a (Å)	4.08685(2)
c (Å)	7.00784(5)
c/a	1.7147
V (Å ³)	101.366(2)
Goodness-of-fit	1.44
R_{wp}	8.41
R_{exp}	5.83
R_p	6.52

E. Magnetic data of FM- and AFM-EuZn₂P₂

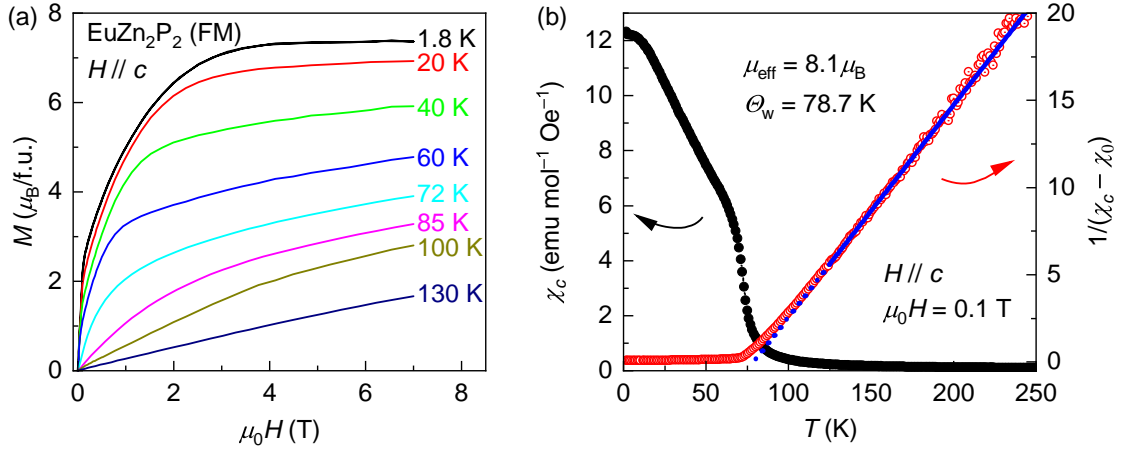


FIG. S4. (a) $M(H)$ curves of FM-EuZn₂P₂ with $H \parallel c$. (b) Curie-Weiss analysis from 125 to 300 K with $\chi_c(T)$ data at 0.1 T.

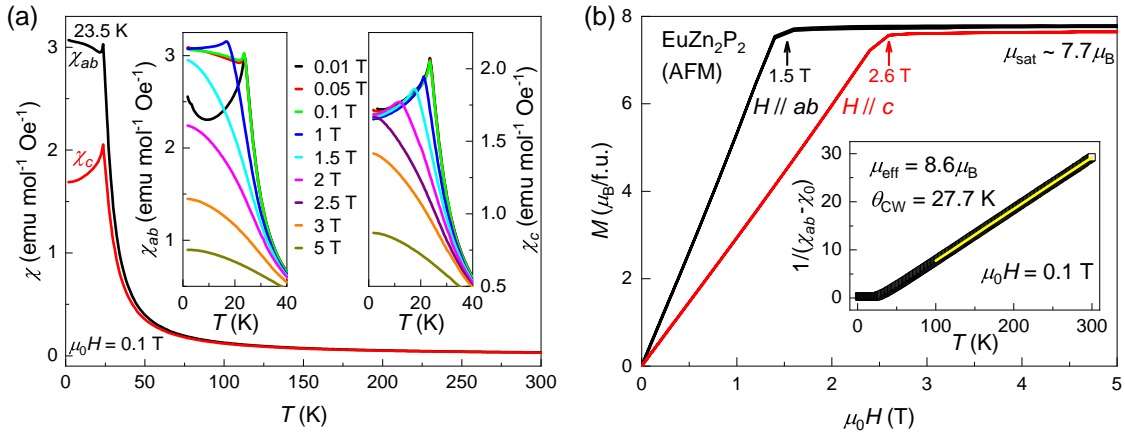


FIG. S5. (a) Temperature dependences of anisotropic magnetic susceptibility for AFM-EuZn₂P₂. $\chi_{ab}(T)$ and $\chi_c(T)$ at 0.1 T are compared in the main panel, while the insets show $\chi(T)$ curves with different fields. (b) Anisotropic magnetizations as a function of field at 1.8 K. Inset shows the Curie-Weiss fit with the in-plane susceptibility.

F. Magnetism of FM-EuZn₂As₂

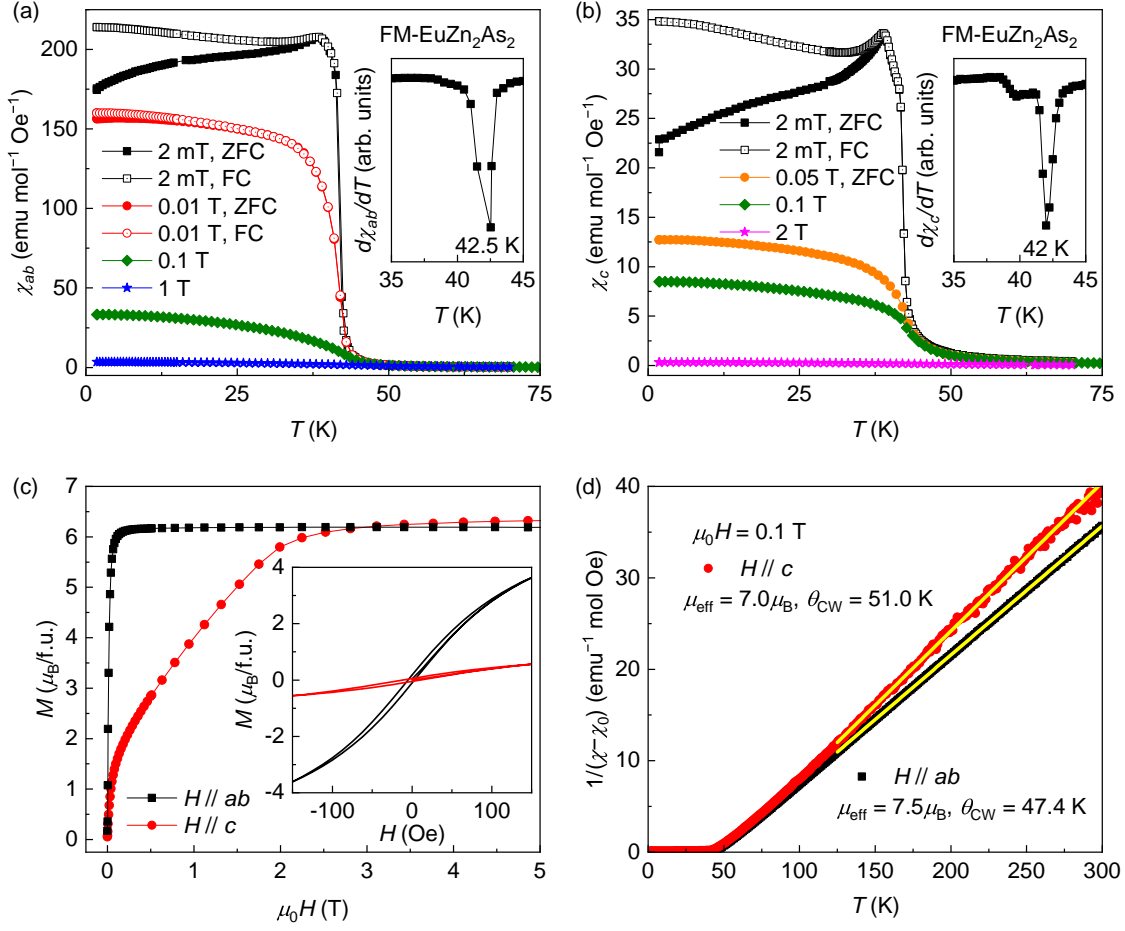


FIG. S6. [(a),(b)] Temperature dependence of magnetic susceptibility with the field in the ab plane and along the c axis. Insets present the transition points determined by the derivative ($d\chi/dT$). (c) Anisotropic magnetizations as a function of field for FM-EuZn₂As₂. Inset shows the hysteresis loops under the low external fields. (d) Curie-Weiss analysis of $\chi(T)$.

G. Magnetism of FM-EuCd₂P₂

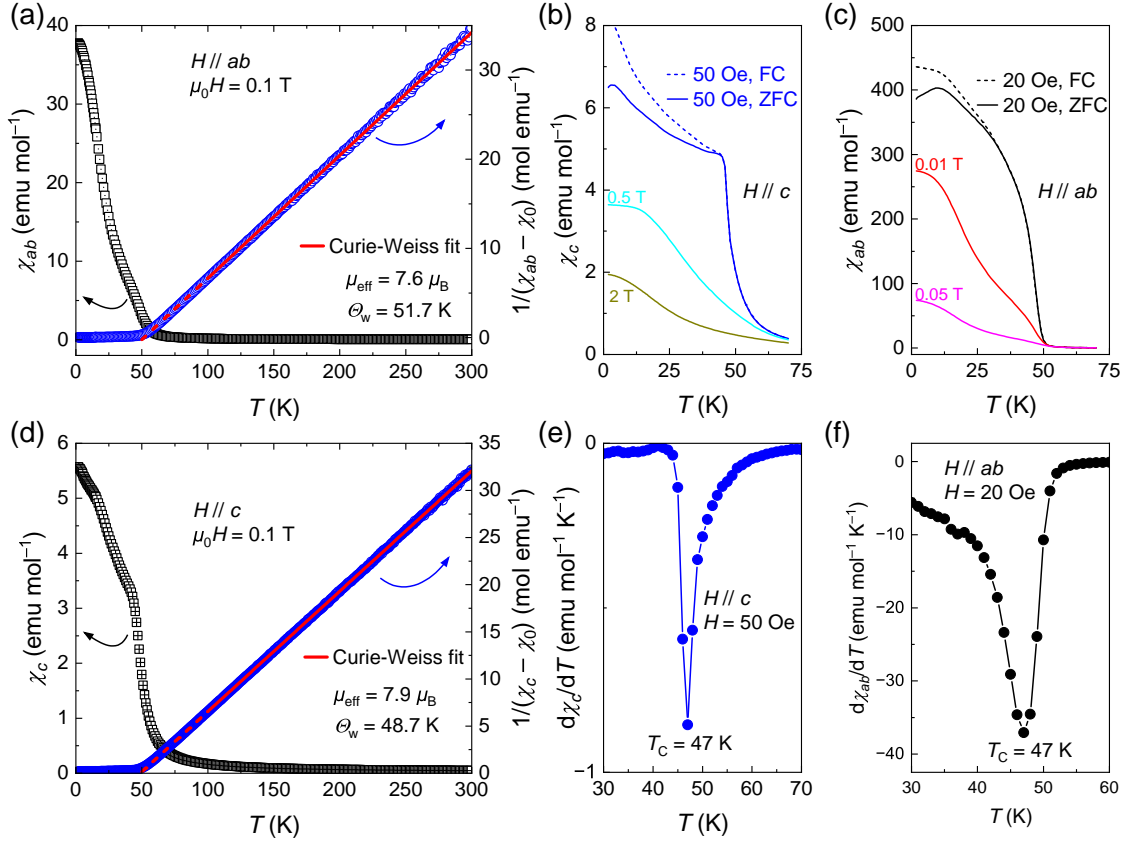


FIG. S7. [(a),(d)] The in-plane and out-of-plane susceptibility measured under 0.1 T (left axes), and the corresponding reciprocal of susceptibility as well as the Curie-Weiss fits from 100 to 300 K (right axes). [(b),(c)] Temperature dependences of magnetic susceptibility $\chi(T)$ in various out-of-plane and in-plane fields. [(e),(f)] Transition temperatures determined by $d\chi_c/dT$ and $d\chi_{ab}/dT$, respectively.

H. SEM images and compositions of FM-EuZn₂As₂

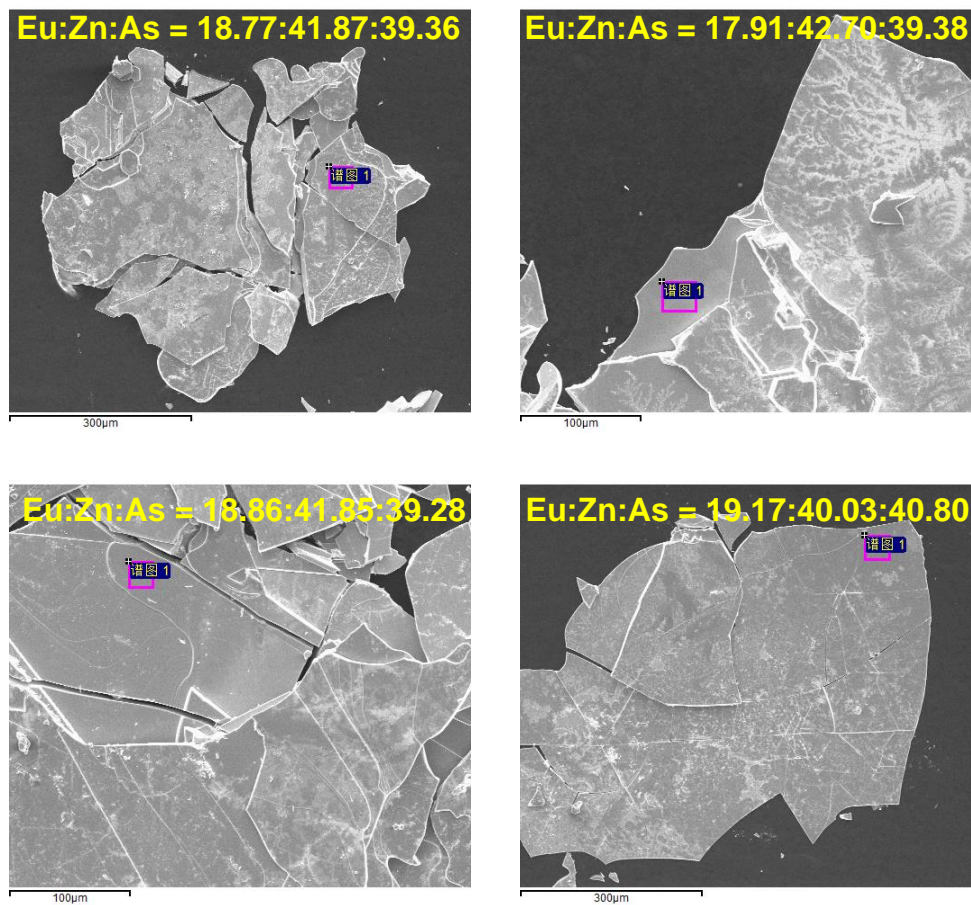


FIG. S8. The SEM images of FM-EuZn₂As₂ single crystals. The compositions collected by EDX are shown as yellow text on the images. The crystals are brittle.